Available online at www.sciencedirect.com
SCIENCE DIRECT®
Journal of Computational Physics 213 (2006) 311–329
JOURNAL OF COMPUTATIONAL PHYSICS
www.elsevier.com/locate/jcp

Simulations of pulsating one-dimensional detonations with true fifth order accuracy ☆

Andrew K. Henrick [a], Tariq D. Aslam [b,*], Joseph M. Powers [a]

[a] Department of Aerospace and Mechanical Engineering, University of Notre Dame, Notre Dame, IN 46556, United States
[b] Dynamic Experimentation Division, Los Alamos National Laboratory, Group DX-2, MS P952, Los Alamos, NM 87545, United States

Received 8 June 2005; received in revised form 12 August 2005; accepted 15 August 2005
Available online 4 October 2005

Abstract

A novel, highly accurate numerical scheme based on shock-fitting coupled with fifth order spatial and temporal discretizations is applied to a classical unsteady detonation problem to generate solutions with unprecedented accuracy. The one-dimensional reactive Euler equations for a calorically perfect mixture of ideal gases whose reaction is described by single-step irreversible Arrhenius kinetics are solved in a series of calculations in which the activation energy is varied. In contrast with nearly all known simulations of this problem, which converge at a rate no greater than first order as the spatial and temporal grid is refined, the present method is shown to converge at a rate consistent with the fifth order accuracy of the spatial and temporal discretization schemes. This high accuracy enables more precise verification of known results and prediction of heretofore unknown phenomena. To five significant figures, the scheme faithfully recovers the stability boundary, growth rates, and wave-numbers predicted by an independent linear stability theory in the stable and weakly unstable regime. As the activation energy is increased, a series of period-doubling events are predicted, and the system undergoes a transition to chaos. Consistent with general theories of non-linear dynamics, the bifurcation points are seen to converge at a rate for which the Feigenbaum constant is 4.66 ± 0.09, in close agreement with the true value of 4.669201.... As activation energy is increased further, domains are identified in which the system undergoes a transition from a chaotic state back to one whose limit cycles are characterized by a small number of non-linear oscillatory modes. This result is consistent with behavior of other non-linear dynamical systems, but not typically considered in detonation dynamics. The period and average detonation velocity are calculated for a variety of asymptotically stable limit cycles. The average velocity for such pulsating detonations is found to be slightly greater than the Chapman–Jouguet velocity.
Published by Elsevier Inc.

Keywords: WENO; Mapped WENO; Detonation; Shock-fitting; Stability; Bifurcation

☆ This study has been supported by Los Alamos National Laboratory and performed under the auspices of the US Department of Energy.

* Corresponding author. Tel.: +1 505 6671367; fax: +1 505 6676372.
E-mail addresses: ahenrick@nd.edu (A.K. Henrick), aslam@lanl.gov (T.D. Aslam), powers@nd.edu (J.M. Powers).

0021-9991/$ - see front matter. Published by Elsevier Inc.
doi:10.1016/j.jcp.2005.08.013

1. Introduction

In this paper, we describe and implement a new algorithm tailored to simulate a well established model problem: one-dimensional unsteady detonation; this study gives full details of recently reported results [1]. The new predictions are many orders of magnitude more precise than those previously published; this enhanced precision enables the prediction of remarkable new bifurcation phenomena. The model on which we focus simulates the key mechanisms of convection and single step exothermic reaction. For tractability, simpler constitutive relations than those which are appropriate for real materials are employed, and all diffusive transport is neglected. Consequently, direct comparison with experimental results will be impossible. However, the techniques described here can, in principle, be adapted to models which better represent actual physical systems with detailed kinetics and complex state equations [2]. Nevertheless, the widely disparate length scales present in such systems pose such a formidable modeling challenge that it is unlikely that a fully resolved unsteady detonation for a system with detailed kinetics exists as of yet [3].

In particular, this study presents numerical predictions of classical pulsating one-dimensional detonations propagating in an inviscid reacting calorically perfect ideal gas whose chemistry is modeled by one-step irreversible kinetics. The numerical solutions formally converge at a fifth order rate so that high accuracy is achieved at a moderate computational cost. The high rate of convergence is obtained using a shock-fitting scheme in which the reactive Euler equations are transformed to a shock-attached frame. A method of lines approach is used to discretize the resulting partial differential equations (PDEs) on a uniform spatial grid [4]. In the interior of the computational domain, spatial gradients are modeled by a fifth order mapped weighted essentially non-oscillatory scheme (WENO5M) [5]. The resulting ordinary differential equations in time are then solved by a fifth order Runge–Kutta technique [6].

Unsteady detonations predicted by the model employed here have been widely studied for over 40 years. A partial list [7–19] summarizes some of the many approaches: linear stability via normal modes analysis, asymptotic techniques, method of characteristics, and direct numerical simulation using shock-capturing, shock-tracking and/or adaptive mesh refinement techniques. Linear stability analysis gives the most rigorous results, but cannot capture the non-linear dynamics or long-time limit cycle behavior. The method of characteristics, when coupled with a high order method for solution of ordinary differential equations, can give accurate results, at the expense of algorithmic complexity and difficulty in accommodating flows with multiple discontinuities. Shock capturing techniques are easy to implement, but results are corrupted by order one errors at the shock which propagate into the entire flow field, rendering it difficult to precisely identify fine scale dynamics [20–23]. Methods which do have high order accuracy for continuous solutions, when coupled with a shock-capturing scheme, always reduce that accuracy to at most first order. Although shock-tracking [8,10,11,17] and shock-fitting schemes [18] can in principle eliminate the order one errors at the shock, high rates of global convergence have not been demonstrated to date.

The potential for highly accurate discontinuous solutions is recovered through shock-fitting, effectively partitioning the domain into two pieces over which the solution is smooth. The discrete method of computing spatial and temporal derivatives for each smooth solution then determines the actual order of accuracy of the method. Thus, it is speculated that shock-fitted solutions can be computed at arbitrarily high orders of accuracy by employing any number of different numerical schemes solving either the conservative or non-conservative forms of the governing equations. Furthermore, the choices are not limited to finite difference methods; spectral methods have also been employed in conjunction with shock-fitting [24–26] in related problems. If desired, our results could easily be extended to a spectral spatial discretization. However, for time-dependent problems, such as we consider, spatially spectral methods are constrained to converge globally at an order no higher than that of the time integration scheme.

The true high order accuracy of the new numerical algorithm is the principal novelty of this work; less accurate versions of most results have appeared previously in the literature. We compare our results with two of the best recent studies: Kasimov and Stewart [18] and Ng et al. [19]. Several test problems are exploited to verify the accuracy of the scheme. In particular, for unstable detonations it becomes possible to predict, with high precision and moderate resolution, both the growth rates and frequencies of the same unstable modes which have been independently predicted by linear stability analysis. The results are then extended into the non-linear regime to predict the ultimate limit cycle behavior. Relative to recent related calculations

[18,19], those presented here are resolved in roughly two orders of magnitude more detail, which allows a clearer elucidation of the structurally rich bifurcation phenomena. In particular, new windows of parameter space are identified in which low frequency behavior is predicted in an otherwise chaotic region.

The plan of the paper is as follows. First, the governing equations and associated jump conditions are specified. An evolution equation for the shock velocity is derived, which is commonly referred to as the shock-change equation [27]. A description of the fifth order scheme is then presented. The solutions to various test problems are given. These include comparisons with the stable Zel'dovich–von Neumann–Döring (ZND) solution, growth rate and frequency of linearly unstable ZND waves, and fully time-dependent and non-linear detonation pulsation flows. A detailed bifurcation diagram shows how the long-time limit of the detonation wave speed behaves as activation energy is varied. Period-doubling bifurcations, identified earlier [14,19], are found to much greater precision, and several new modes of behavior are given. It is also confirmed that the convergence of the period-doubling bifurcation points is in agreement with the general theory of Feigenbaum [28,29]. The limit cycle period and average detonation speed are given for asymptotically stable flows with a variety of activation energies; the average detonation speed is found to be slightly greater than the Chapman–Jouguet (CJ) speed.

2. Governing equations

The one-dimensional unsteady reactive Euler equations for a calorically perfect ideal gas which undergoes a single irreversible reaction are expressed in conservative form as

$$\frac{\partial \rho}{\partial t} + \frac{\partial}{\partial \xi}(\rho u) = 0, \tag{1a}$$

$$\frac{\partial}{\partial t}(\rho u) + \frac{\partial}{\partial \xi}(\rho u^2 + p) = 0, \tag{1b}$$

$$\frac{\partial}{\partial t}\left(\rho\left(e + \frac{1}{2}u^2\right)\right) + \frac{\partial}{\partial \xi}\left(\rho u\left(e + \frac{1}{2}u^2 + \frac{p}{\rho}\right)\right) = 0, \tag{1c}$$

$$\frac{\partial}{\partial t}(\rho\lambda) + \frac{\partial}{\partial \xi}(\rho u\lambda) = k\rho(1-\lambda)\exp\left(-\frac{\rho E}{p}\right), \tag{1d}$$

$$e = \frac{1}{\gamma - 1}\frac{p}{\rho} - \lambda q. \tag{1e}$$

Here, the laboratory frame Cartesian spatial coordinate is ξ, and time is t. The dependent variables in Eqs. (1) are density ρ, particle velocity u, pressure p, specific internal energy e, and reaction progress λ. The parameters are the reaction kinetic rate constant k, activation energy E, ratio of specific heats γ, and heat release per unit mass q. Eqs. (1) are expressions of, respectively, the conservation of mass, ξ-momentum, and energy, evolution of species, and a caloric state relation. Eq. (1d) models the irreversible reaction $A \rightarrow B$ in which species A and B have identical molecular masses and specific heats. The mass fractions of each species, Y_A and Y_B, are given in terms of the reaction progress variable by the relations $Y_A = 1-\lambda$ and $Y_B = \lambda$.

Eqs. (1) are supplemented by the following standard Rankine–Hugoniot conditions at the shock jump:

$$\rho_s(D(t) - u_s) = \rho_o(D(t) - u_o), \tag{2a}$$

$$p_s - p_o = (\rho_o(D(t) - u_o))^2\left(\frac{1}{\rho_o} - \frac{1}{\rho_s}\right), \tag{2b}$$

$$e_s - e_o = \frac{1}{2}(p_s + p_o)\left(\frac{1}{\rho_o} - \frac{1}{\rho_s}\right), \tag{2c}$$

$$\lambda_s = \lambda_o. \tag{2d}$$

Here, D is the shock velocity, which in general is time-dependent; the subscript s denotes the shock state, and the subscript o denotes the constant ambient state. Note that the shock states in Eqs. (2) can be determined in terms of the ambient state and the shock velocity. It is assumed that no reaction takes place upstream of the shock; i.e., the source term in Eq. (1d) is activated only for fluid particles which have passed through the shock.

For the shock-fitting numerical scheme, Eqs. (1) are transformed to a frame that is fixed to the shock front. To this end, a new spatial variable is taken to be

$$x = \xi - \int_0^t D(\tau)\,\mathrm{d}\tau, \tag{3}$$

where the shock is initially presumed to be at $\xi = 0$, and thus for all time the shock locus is $x = 0$. Under this transformation, one recovers the following conservation laws:

$$\frac{\partial \rho}{\partial t} + \frac{\partial}{\partial x}(\rho(u - D)) = 0, \tag{4a}$$

$$\frac{\partial}{\partial t}(\rho u) + \frac{\partial}{\partial x}(\rho u(u - D) + p) = 0, \tag{4b}$$

$$\frac{\partial}{\partial t}\left(\rho\left(e + \frac{1}{2}u^2\right)\right) + \frac{\partial}{\partial x}\left((u - D)\rho\left(e + \frac{1}{2}u^2\right) + up\right) = 0, \tag{4c}$$

$$\frac{\partial}{\partial t}(\rho\lambda) + \frac{\partial}{\partial x}(\rho(u - D)\lambda) = k\rho(1 - \lambda)\exp\left(-\frac{\rho E}{p}\right). \tag{4d}$$

The particle velocity, u, is still measured in the laboratory frame. Up to this point, there is nothing different from earlier shock-fitting formulations [18].

Eqs. (4) do not yet form a complete system of equations; an expression for the change in shock velocity, D, with time is still required. In order to close the system, consider that the boundary condition provided at the shock by Eqs. (2) is a function of D alone for a given ambient state. Thus, the state variables are all coupled through D at the shock and cannot evolve independently if they are to satisfy the boundary condition; however, Eqs. (2) can also be solved to find an expression for the shock velocity in terms of the state variables at the shock. This observation combined with the governing PDEs provides the basis for the derivation of the shock velocity evolution equation, otherwise known as the shock-change equation [27].

2.1. Shock-change equation

The shock-change equation describes the evolution of the shock velocity as a function of time. This relationship can take on various forms which are mathematically equivalent. A new and particularly useful form is derived here. First, assuming $\lambda_\mathrm{o} = 0$, one determines the momentum at the shock state from Eqs. (1) and (2) to be

$$\rho_\mathrm{s} u_\mathrm{s} = \frac{\rho_\mathrm{o}(D - u_\mathrm{o})(\gamma(\rho_\mathrm{o}(D - u_\mathrm{o})u_\mathrm{o} - 2p_\mathrm{o}) + \rho_\mathrm{o}(2D^2 - 3Du_\mathrm{o} + u_\mathrm{o}^2))}{\gamma(2p_\mathrm{o} + \rho_\mathrm{o}(D - u_\mathrm{o})^2) - \rho_\mathrm{o}(D - u_\mathrm{o})^2}. \tag{5}$$

As $\rho_\mathrm{s} u_\mathrm{s}$ in Eq. (5) is a function of D alone, one has

$$\frac{\mathrm{d}D}{\mathrm{d}t} = \left(\frac{\mathrm{d}(\rho_\mathrm{s} u_\mathrm{s})}{\mathrm{d}D}\right)^{-1} \frac{\mathrm{d}}{\mathrm{d}t}(\rho_\mathrm{s} u_\mathrm{s}), \tag{6}$$

from the chain rule. Note that the derivative of the momentum at the shock with respect to the shock velocity, $\mathrm{d}(\rho_\mathrm{s} u_\mathrm{s})/\mathrm{d}D$, can be obtained in closed form from Eq. (5) but is omitted here due to its complexity. Thus, the only term remaining in Eq. (6) to compute is $\mathrm{d}(\rho_\mathrm{s} u_\mathrm{s})/\mathrm{d}t$.

Now

$$\frac{\mathrm{d}}{\mathrm{d}t}(\rho_\mathrm{s} u_\mathrm{s}) = \left.\frac{\mathrm{d}}{\mathrm{d}t}\right|_{x=0}(\rho u) \tag{7}$$

is the intrinsic derivative of the momentum following the shock. This derivative is given by

$$\left.\frac{\mathrm{d}}{\mathrm{d}t}\right|_{x=0} = \left.\frac{\partial}{\partial t}\right|_{x=0} + \underbrace{\left.\frac{\mathrm{d}x}{\mathrm{d}t}\right|_{x=0}}_{=0}\left.\frac{\partial}{\partial x}\right|_{x=0} = \left.\frac{\partial}{\partial t}\right|_{x=0}, \tag{8}$$

since the velocity of the shock in the fitted coordinate system is zero. Thus, at the shock, rearrangement of Eq. (4b) gives

$$\left.\frac{\mathrm{d}(\rho_s u_s)}{\mathrm{d}t}\right|_{x=0} = -\frac{\partial}{\partial x}(\rho u(u-D)+p)|_{x=0}, \tag{9}$$

the intrinsic derivative of the momentum following the shock in terms of a spatial derivative at the shock. Lastly, substituting Eq. (9) into Eq. (6) yields the shock-change equation

$$\frac{\mathrm{d}D}{\mathrm{d}t} = -\left(\frac{\mathrm{d}(\rho_s u_s)}{\mathrm{d}D}\right)^{-1}\left(\frac{\partial}{\partial x}(\rho u(u-D)+p)\right)\Bigg|_{x=0}. \tag{10}$$

Eq. (10) relates the shock acceleration to the momentum flux gradient at the shock. Other, mathematically equivalent forms of the shock-change equation could have been used, but there are two reasons this particular form was chosen. First, the momentum flux gradient is a quantity that will already be computed throughout the flow, eliminating the need to perform a special characteristic decomposition of the equations at the shock [18,24]. More importantly, it scales easily with shock velocity, so that the first term on the right-hand side of Eq. (10) is well behaved in both the weak and strong shock limits; this quality would not be exhibited if mass rather than momentum conservation was used to derive the shock-change equation. Other combinations of the equations may also be amenable in these limits, but Eq. (10) is adequate for what follows in the next section.

3. Numerical method

Here, the details of the high order shock-fitting numerical algorithm are presented. A point-wise method of lines approach [4] is used. This method simplifies the required coding, allows separate temporal and spatial discretizations, and also allows for the incorporation of source terms. In the following sections, the computational grid will be defined, the WENO5M spatial discretization scheme [5] will be outlined, and the temporally fifth order Runge–Kutta scheme [6] will be given.

Written in vector notation, Eqs. (4) take the form

$$\frac{\partial}{\partial t}\mathbf{u} + \frac{\partial}{\partial x}\mathbf{f}(\mathbf{u}) = \mathbf{s}(\mathbf{u}). \tag{11}$$

Here, the vector $\mathbf{u}$ is used to denote the set of conserved-dependent variables,

$$\mathbf{u} = \left(\rho, \rho u, \rho\left(e+\frac{1}{2}u^2\right), \rho\lambda\right)^{\mathrm{T}}. \tag{12}$$

Strictly speaking, $\rho\lambda$ is not conserved, but evolves due to the reaction source term. It is traditional to label it a conserved variable as well, as it arises from the proper divergence formulation of the reaction kinetics model. The vector $\mathbf{f}$ is a set of fluxes of each conserved quantity, and $\mathbf{s}$ is a source.

3.1. Grid

A uniform Cartesian grid is used to discretize the domain $x \in [x_{\min}, x_{\max}]$, with $N_x + 1$ equally spaced nodes, $x_{\min} < 0$, and $x_{\max} = 0$. One allows the semi-discretizations $\mathbf{u}(x,t) \to \mathbf{u}_i(t)$ and $\mathbf{u}(x,t) \to \mathbf{u}^n(x)$ as well as the full discretization $\mathbf{u}_i(t) \to \mathbf{u}_i^n$ of the solution vector $\mathbf{u}$. Here, i is the spatial node number corresponding to the location $x_i = x_{\min} + i\Delta x$, where $\Delta x = -x_{\min}/N_x$, and n is the time level corresponding to $t_n = \sum_{m=1}^{n}\Delta t_m$, where Δt_m is the time step for each integration step. Half indices are used to denote the spatial midpoint between nodes across which the fluxes are calculated: $i \pm 1/2$ corresponds to the midpoint between nodes i and $i \pm 1$.

3.2. Spatial discretization

Following spatial discretization, Eq. (11) can be approximated as a system of ordinary differential equations in t:

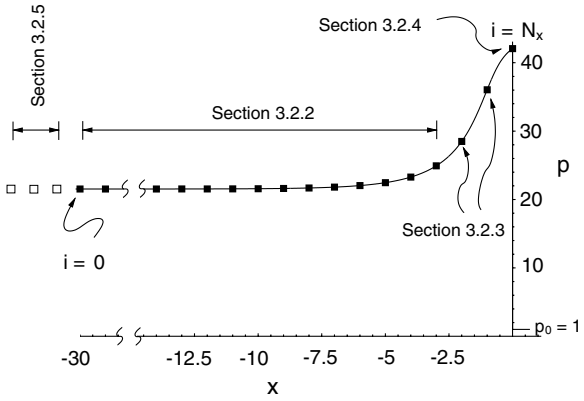

Fig. 1. Artificially coarse numerical grid highlighting boundary points. The section detailing the spatial discretization used at each node is also given. The pressure profile shown is that of the ZND solution used as an initial condition for the case $E = 25$, $q = 50$, and $\gamma = 1.2$.

$$\frac{\mathrm{d}\mathbf{u}_i}{\mathrm{d}t} = \mathbf{L}(\mathbf{u})|_{x=x_i}, \tag{13}$$

where the operator $\mathbf{L}$ is a discrete approximation to the continuous convection and source operators of Eq. (11):

$$\mathbf{L}(\mathbf{u})|_{x=x_i} \approx \left(-\frac{\partial}{\partial x}\mathbf{f}(\mathbf{u}) + \mathbf{s}(\mathbf{u}) \right)\Bigg|_{x=x_i}. \tag{14}$$

It is understood that the evaluation of the discrete spatial operator $\mathbf{L}(\mathbf{u})$ at x_i will involve values of $\mathbf{u}$ other than just $\mathbf{u}_i$.

In this section, the definition of $\mathbf{L}$ for various nodes is given as shown in Fig. 1. First, however, the essentially non-oscillatory high order numerical flux interpolator employed in this scheme is described.

3.2.1. WENO5M

A weighted essentially non-oscillatory scheme is used to approximate spatial derivatives. Besides its essentially non-oscillatory character over both smooth and discontinuous solutions, such schemes are conservative and guarantee that captured shocks will propagate at the correct speeds. This is important for studying unstable detonations since secondary shocks can form in the flow behind the lead shock and cause simpler finite differencing schemes to become unstable. One should note that, in spite of the fact that such secondary shocks are not fitted, the scheme presented here retains its high order accuracy at least throughout the domain of dependence of the fitted shock: from $x = 0$ to the limiting characteristic [18,30].

In particular, the fifth order WENO5M scheme developed in [5] is used. In order to encapsulate the complexity of the method, the WENO5M scheme is presented simply as a special interpolator:

$$\hat{f}_{j+1/2} = \begin{cases} \mathscr{F}(f_{j-2}, f_{j-1}, \ldots, f_{j+2}) & \text{for } \rightarrow \text{ waves,} \quad \text{(a)} \\ \mathscr{F}(f_{j+3}, f_{j+2}, \ldots, f_{j-1}) & \text{for } \leftarrow \text{ waves.} \quad \text{(b)} \end{cases} \tag{15}$$

Both Eqs. (15) give an approximation of the numerical flux function [5,31] at $j + 1/2$ such that a high order conservative discretization of spatial derivatives can be formed. The difference between Eqs. (15) lies in the selection and ordering of the functional arguments. Eq. (15a) propagates information to the right, while Eq. (15b) propagates information to the left. This distinction will become important in the creation of a stable numerical scheme for systems involving the propagation of waves simultaneously in both directions.

Given the values of a function f at the specified nodes, the WENO5M interpolant $\hat{f}_{j+1/2}$ can be computed. The functional form of $\mathscr{F}$ is given by

$$\mathscr{F}(f_{j-2}, f_{j-1}, \ldots, f_{j+2}) = \sum_{k=0}^{2} \omega_k q_k, \tag{16}$$

where the ω_k's are the WENO5M weights and the component stencils q_k are

$$q_0 = \frac{1}{6}(2f_{j-2} - 7f_{j-1} + 11f_j), \tag{17a}$$

$$q_1 = \frac{1}{6}(-f_{j-1} + 5f_j + 2f_{j+1}), \tag{17b}$$

$$q_2 = \frac{1}{6}(2f_j + 5f_{j+1} - f_{j+2}). \tag{17c}$$

Next, the formulation of the ω_k's is given in two steps.

As a first approximation of the final weights, those developed in [31] are calculated. These are given by

$$\omega_k^* = \frac{\alpha_k}{\sum_{i=0}^{2}\alpha_i}, \quad \text{where } \alpha_k = \frac{\bar{\omega}_k}{(\epsilon + \beta_k)^p}. \tag{18}$$

The ideal weights, $\bar{\omega}_k$, are constants given by

$$\bar{\omega}_0 = 1/10, \quad \bar{\omega}_1 = 6/10, \quad \bar{\omega}_2 = 3/10, \tag{19}$$

and the indicators of smoothness, β_k, are defined as

$$\beta_0 = \frac{13}{12}(f_{j-2} - 2f_{j-1} + f_j)^2 + \frac{1}{4}(f_{j-2} - 4f_{j-1} + 3f_j)^2, \tag{20a}$$

$$\beta_1 = \frac{13}{12}(f_{j-1} - 2f_j + f_{j+1})^2 + \frac{1}{4}(f_{j+1} - f_{j-1})^2, \tag{20b}$$

$$\beta_2 = \frac{13}{12}(f_j - 2f_{j+1} + f_{j+2})^2 + \frac{1}{4}(3f_j - 4f_{j+1} + f_{j+2})^2. \tag{20c}$$

Here, ϵ is the small parameter which keeps the weights bounded. In all computations presented here, $\epsilon = 10^{-40}$, as suggested in [5].

Next, the ω_k^*'s are mapped to the corrected ω_k's, such that the accuracy of the method is fifth order in general. This is done through the mappings

$$g_k(\omega) = \frac{\omega(\bar{\omega}_k + \bar{\omega}_k^2 - 3\bar{\omega}_k\omega + \omega^2)}{\bar{\omega}_k^2 + (1 - 2\bar{\omega}_k)\omega}. \tag{21}$$

The final corrected weights are given by

$$\omega_k = \frac{g_k(\omega_k^*)}{\sum_{i=0}^{2} g_i(\omega_i^*)}. \tag{22}$$

3.2.2. Nodes $0 \leqslant i \leqslant N_x - 3$

Next, general nodes in the interior of the domain are considered. For $\mathbf{L}(\mathbf{u})|_{x=x_i}$ the WENO5M scheme [5] with a local Lax–Friedrichs solver is used. This scheme is a conservative flux difference method, which has been shown to be stable, and yields the proper viscosity-vanishing solution to Eqs. (1). The derivation of the difference operator $\mathbf{L}(\mathbf{u})|_{x=x_i}$ in Eq. (14) is done in two parts. First the flux is split into two parts representing right and left moving waves. Then each of these fluxes is numerically approximated using the WENO5M discretization. The final form of the operator is then given in a simplified form.

First, a local Lax–Friedrichs flux splitting of the spatial derivative in Eq. (14) gives

$$\left.\frac{\partial \mathbf{f}}{\partial x}\right|_{x=x_i} = \frac{1}{2}\left.\left(\frac{\partial \mathbf{f}^+}{\partial x} + \frac{\partial \mathbf{f}^-}{\partial x}\right)\right|_{x=x_i}, \tag{23}$$

where

$$\mathbf{f}_i^{\pm} = \mathbf{f}_i \pm \alpha \mathbf{u}_i, \tag{24}$$

and α is the largest local wave speed in an absolute value sense. This splitting yields $\mathbf{f}_i^+$ and $\mathbf{f}_i^-$ which correspond to the flux vectors for right and left moving waves, respectively.

Next the flux derivatives in Eq. (23) are approximated at each node i by

$$\left.\frac{\partial \mathbf{f}^{\pm}}{\partial x}\right|_{x=x_i} = \frac{\hat{\mathbf{f}}^{\pm}_{i+1/2} - \hat{\mathbf{f}}^{\pm}_{i-1/2}}{\Delta x} + \mathrm{O}(\Delta x^5), \tag{25}$$

where $\hat{\mathbf{f}}^{\pm}_{i\pm1/2}$ is the WENO5M interpolant of $f^{\pm}$ at $i \pm 1/2$. For the $i+1/2$ case, application of Eqs. (15) gives

$$\begin{aligned} \hat{f}^{+}_{i+1/2} &= \mathscr{F}\left(f^{+}_{i-2}, f^{+}_{i-1}, f^{+}_{i}, f^{+}_{i+1}, f^{+}_{i+2}\right), \\ \hat{f}^{-}_{i+1/2} &= \mathscr{F}\left(f^{-}_{i+3}, f^{-}_{i+2}, f^{-}_{i+1}, f^{-}_{i}, f^{-}_{i-1}\right), \end{aligned} \tag{26}$$

where either Eq. (15a) or Eq. (15b) has been chosen to match the direction of information propagation for the f^{+} and f^{-} waves, respectively.

Substitution of Eq. (25) into Eq. (23) gives

$$\begin{aligned} \left.\frac{\partial \mathbf{f}}{\partial x}\right|_{x=x_i} &= \frac{1}{2}\left(\frac{\hat{\mathbf{f}}^{+}_{i+1/2} - \hat{\mathbf{f}}^{+}_{i-1/2}}{\Delta x} + \frac{\hat{\mathbf{f}}^{-}_{i+1/2} - \hat{\mathbf{f}}^{-}_{i-1/2}}{\Delta x}\right) + \mathrm{O}(\Delta x^5) \\ &= \frac{1}{\Delta x}\left(\frac{\hat{\mathbf{f}}^{+}_{i+1/2} + \hat{\mathbf{f}}^{-}_{i+1/2}}{2} - \frac{\hat{\mathbf{f}}^{+}_{i-1/2} + \hat{\mathbf{f}}^{-}_{i-1/2}}{2}\right) + \mathrm{O}(\Delta x^5) \\ &= \frac{\hat{\mathbf{f}}_{i+1/2} - \hat{\mathbf{f}}_{i-1/2}}{\Delta x} + \mathrm{O}(\Delta x^5), \end{aligned} \tag{27}$$

where

$$\hat{\mathbf{f}}_{i+1/2} = \frac{1}{2}\left(\hat{\mathbf{f}}^{+}_{i+1/2} + \hat{\mathbf{f}}^{-}_{i+1/2}\right) \tag{28}$$

defines a single value for the approximate numerical flux in between nodes i and $i+1$. Since Eq. (28) gives the numerical flux approximations midway between each node i and $i+1$ in this domain, it is only necessary to formulate the interpolant for the $i+1/2$ case; the $i-1/2$ case is given simply by shifting i by -1.

The numerical flux given by Eq. (28) is calculated using values of f^{+} and f^{-} as given in Eq. (24) where α can now be defined locally as

$$\alpha = \max\left(\left\|\frac{\partial \mathbf{f}}{\partial \mathbf{u}}\right\|_{x=x_i}, \left\|\frac{\partial \mathbf{f}}{\partial \mathbf{u}}\right\|_{x=x_{i+1}}\right), \tag{29}$$

where the norm of the Jacobian matrix, $\partial \mathbf{f}/\partial \mathbf{u}$, is the largest eigenvalue in an absolute value sense.

Substitution of Eq. (27) into Eq. (14) gives the definition of $\mathbf{L}$ in the interior of the domain:

$$\mathbf{L}(\mathbf{u})|_{x=x_i} = -\frac{\hat{\mathbf{f}}_{i+1/2} - \hat{\mathbf{f}}_{i-1/2}}{\Delta x} + \mathbf{s}(\mathbf{u}_i), \tag{30}$$

where $\mathbf{s}(\mathbf{u}_i)$ is a simple evaluation of the source terms at node x_i.

Because the WENO5M discretization at node i requires information at the nodes $i-3, \ldots, i+3$, fluxes at the three nodes in the neighborhood of the shock are calculated separately. For these nodes, either a discretization is used which does not require information differencing across the fitted shock or the shock jump conditions Eqs. (2) are used directly.

3.2.3. Nodes $N_x - 2 \leqslant i \leqslant N_x - 1$

At these nodes, the flux derivatives are approximated by explicit formula biased in such a manner that no nodes $i > N_x$ are used. These are derived from standard Taylor series expansions (TSE). These approximations are given by

$$\frac{\partial}{\partial x}\left(f(\mathbf{u}_{N_x-2})\right) \approx \frac{1}{60\Delta x}\left(-2f(\mathbf{u}_{N_x-5}) + 15f(\mathbf{u}_{N_x-4}) - 60f(\mathbf{u}_{N_x-3}) + 20f(\mathbf{u}_{N_x-2}) + 30f(\mathbf{u}_{N_x-1}) - 3f(\mathbf{u}_{N_x})\right), \tag{31}$$

and

$$\frac{\partial}{\partial x}(f(\mathbf{u}_{N_x-1})) \approx \frac{1}{12\Delta x}(-f(\mathbf{u}_{N_x-4}) + 6f(\mathbf{u}_{N_x-3}) - 18f(\mathbf{u}_{N_x-2}) + 10f(\mathbf{u}_{N_x-1}) + 3f(\mathbf{u}_{N_x})). \tag{32}$$

According to TSE, Eq. (31) is fifth order accurate, while Eq. (32) is fourth order accurate. Use of this fourth order stencil at node $N_x - 1$ appears necessary to ensure linear numerical stability; however, no noticeable loss in the global fifth order convergence rate of the scheme is incurred (see Sections 4.1 and 4.5). Since the line $\xi(x_{N_x-1}, t)$ is not along a characteristic, the fourth order spatial errors suffered at this line do not accumulate along any one characteristic solution. The source term, $\mathbf{s}(\mathbf{u}_i)$, is still just an evaluation at these two nodes.

3.2.4. Node $i = N_x$

At the shock locus, $i = N_x$, the solution is only a function of the shock velocity, D. At this point, only Eq. (10) is solved. Only the momentum flux gradient needs to be computed to update the shock velocity. Here, a biased fifth order stencil,

$$\frac{\partial}{\partial x}(f(\mathbf{u}_{N_x})) \approx \frac{1}{60\Delta x}(-12f(\mathbf{u}_{N_x-5}) + 75f(\mathbf{u}_{N_x-4}) - 200f(\mathbf{u}_{N_x-3}) + 300f(\mathbf{u}_{N_x-2}) - 300f(\mathbf{u}_{N_x-1}) + 137f(\mathbf{u}_{N_x})), \tag{33}$$

is used to calculate the momentum flux gradient.

The conservative state variables at the shock are given from the shock jump relations, Eqs. (2). No source terms enter at this nodal point, since this is exactly a shock state. Also, the numerical method is discretely conservative everywhere, except at $i = N_x$, since the state there is constrained to be at a shock state, and so itself cannot be discretely conservative. Errors in conservation are of the order of the truncation error of the scheme, and so are small.

3.2.5. Nodes $i < 0$

At nodes for which $i < 0$, which are necessary for calculation of some fluxes, a zero gradient condition is enforced. Formally, this introduces spurious waves at the boundary. However, as a check, the forward characteristic emanating from this boundary was calculated, and it was guaranteed that the domain was sufficiently large so as to prevent corruption of the shock and reaction zone structure from this downstream acoustic noise.

3.3. Temporal discretization

With the discrete operator $\mathbf{L}$ now defined, Eqs. (13) could be solved by a wide variety of standard numerical techniques, explicit or implicit, which have been developed over the years for large systems of ordinary differential equations. Here, an explicit 6-stage Runge–Kutta scheme [6] with fifth order temporal accuracy is chosen.

Most Runge–Kutta schemes of fourth or higher order are easier to code and seem to require less storage when the Butcher formulation [6,32] is chosen rather than the more commonplace $\alpha - \beta$ form [4]. Given a solution $\mathbf{u}_i^n$ at t_n, the solution $\mathbf{u}_i^{n+1}$ at t_{n+1} is constructed in the following manner. The generic s-stage Butcher formulation of Runge–Kutta schemes takes the form

$$\begin{aligned} \bar{\mathbf{u}}_i^1 &= \mathbf{u}_i^n, \\ \bar{\mathbf{u}}_i^j &= \mathbf{u}_i^n + \Delta t_n \sum_{k=1}^{j-1} a_{jk} \mathbf{L}(\bar{\mathbf{u}}^k)|_{x=x_i}, \end{aligned} \tag{34}$$

where $\bar{\mathbf{u}}_i^j$ are the intermediate solution states at each j-stage, and the solution at the next time step is given by

$$\mathbf{u}_i^{n+1} = \mathbf{u}_i^n + \Delta t_n \sum_{j=1}^{s} b_j \mathbf{L}(\bar{\mathbf{u}}^j)|_{x=x_i}. \tag{35}$$

The coefficients, a_{jk} and b_j in Eqs. (34) and (35), are given in Tables 1 and 2, respectively.

In this problem, for which the effect of the source term has been resolved, it is convection which dictates the time step restriction. All computations performed here have $0.8 < CFL < 1.5$, where CFL represents the traditional Courant–Friedrichs–Lewy number. The high order of the Runge–Kutta method enables CFL to be slightly greater than unity while maintaining numerical stability. The results were verified to be insensitive to small changes in CFL.

4. Results

Results are given for a set of standard test cases. All calculations were performed on a 2 GHz Apple Power Mac G5 using double precision and 64-bit arithmetic. The typical computation time for any single case was 10 min. A few calculations which required long integration times took as long as two weeks to complete. The equations have been scaled in such a fashion that the ambient density and pressure are $\rho_o = 1$ and $p_o = 1$, the half-reaction zone length, $L_{1/2}$, is unity, and other parameters take the values $q = 50$, and $\gamma = 1.2$. Here, $L_{1/2}$ is the distance from the shock to the point at which λ takes the value 1/2 for the steady ZND structure. This now standard approach requires one to vary k from case to case in order to maintain $L_{1/2} = 1$; for $E = 25$, one has $k = 35.955584760859722$, where the high precision is needed to guarantee the high precision of the results.

Here, interest is focused on self-sustained CJ detonation waves [27]. This results in a steady detonation velocity of

$$D_{CJ} = \sqrt{11} + \sqrt{\frac{61}{5}} \approx 6.80947463. \tag{36}$$

Interest is further focused on how increase in the activation energy, E, affects the propagation of the detonation wave. Linear stability analysis [9] reveals that for $E < 25.26$, the steady ZND detonation wave structure [27] will be linearly stable, and for $E > 25.26$, the steady detonation structure is linearly unstable. In all cases considered, the exact, to machine precision, ZND solution is used as the initial condition. Note that using 64-bit machine precision translates to roughly 16 significant figures. A second comparison case is presented in the following subsection for $E = 26$.

In all unstable cases considered, the predicted non-linear behavior has its origin in a single unstable low frequency mode identified by linear theory. While evermore high frequency modes are predicted by the linear theory as E increases through a series of threshold values, here, E is increased only moderately. As a consequence, the high frequency instabilities are not activated, while still admitting a rich spectrum of low frequency non-linear behavior.

Table 1
Runge–Kutta coefficients a_{jk}

	$k=1$	$k=2$	$k=3$	$k=4$	$k=5$
$j=2$	1				
$j=3$	$\frac{1}{4}$	$\frac{1}{4}$			
$j=4$	$\frac{2046}{15625}$	$-\frac{454}{15625}$	$\frac{1533}{15625}$		
$j=5$	$-\frac{739}{5625}$	$\frac{511}{5625}$	$-\frac{566}{16875}$	$\frac{20}{27}$	
$j=6$	$\frac{11822}{21875}$	$-\frac{6928}{21875}$	$-\frac{4269}{21875}$	$-\frac{4}{7}$	$\frac{54}{35}$

Table 2
Runge–Kutta coefficients b_j

$b_1 = \frac{1}{24}$
$b_2 = 0$
$b_3 = 0$
$b_4 = \frac{125}{336}$
$b_5 = \frac{27}{56}$
$b_6 = \frac{5}{48}$

4.1. Linearly stable ZND, $E = 25$

The new algorithm is first tested on a stable problem, $E = 25$, and results are compared with those of a recent shock-fitting study [18]. For this case, the steady solution is stable, and thus it is the exact solution for all time. This can also serve as a test problem for verification of the numerical scheme. As done in [18] the numerically calculated detonation velocity can be plotted as a function of time. In particular, it is important to measure the error produced as a function of numerical resolution. Following [18], one defines the number of numerical zones in the half reaction zone length to be $N_{1/2}$, so that $\Delta x = 1/N_{1/2}$. Fig. 2 shows the result of Kasimov and Stewart's numerical method for $N_{1/2} = 100$ and $N_{1/2} = 200$. At relatively long times, this numerical method attains $D_{N_{1/2}=100} \approx 6.8285$ and $D_{N_{1/2}=200} \approx 6.8189$. Considering the numerical errors, ΔD, are then 0.0190 and 0.0094, respectively, it is concluded that the error of the scheme of [18] scales directly with Δx, and is thus first order accurate. These results are summarized in Table 3, where r_c is the rate of convergence. The lack of high order convergence is due to the first order finite differencing of the shock-change equations.

The prediction of the high order shock-fitting algorithm of the previous section, utilizing a coarser grid, $N_{1/2} = 20$, is displayed in Fig. 3. A few important facts should be noted. First, the error in shock speed has been greatly reduced by the high order shock-fitting scheme, even utilizing a much coarser grid. This is evident because of greatly reduced scale on the detonation velocity in Fig. 3. Also, not only are the errors greatly reduced, but the rate of convergence is shown to be fifth order as seen in Table 4. Thus, for this stable problem, the new high order shock-fitting scheme produces very accurate solutions with moderate mesh size.

4.2. Linearly unstable ZND, stable limit cycle, $E = 26$

Next, an unstable problem, $E = 26$, is analyzed, as also done in [18]. For $E = 26$, linear stability theory [14] predicts a single unstable mode, with growth rate, $\sigma_r = 0.03710$, and a frequency, $\sigma_i = 0.52215$. Fig. 4 gives a plot of the numerical prediction of detonation velocity, D, as a function of time, with $N_{1/2} = 20$. The growth of the unstable mode is triggered by the small numerical truncation error. Fig. 4 shows a clearly oscillatory

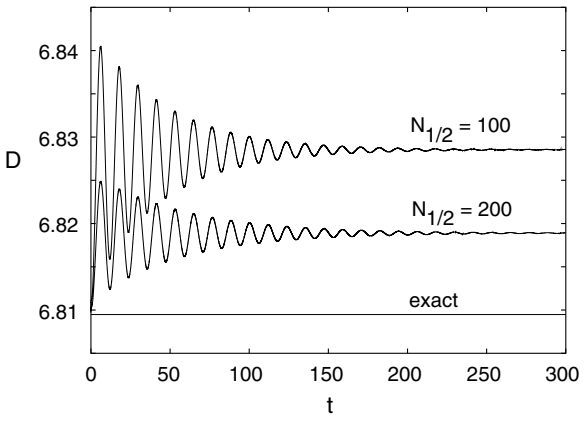

Fig. 2. Numerically generated detonation velocity, D versus t, using the shock-fitting scheme of Kasimov and Stewart [18], $E = 25$, $q = 50$, $\gamma = 1.2$, with $N_{1/2} = 100$ and $N_{1/2} = 200$.

Table 3
Numerical accuracy of algorithm presented in [18]

$N_{1/2}$	ΔD	r_c
100	1.90×10^{-2}	–
200	9.40×10^{-3}	1.01

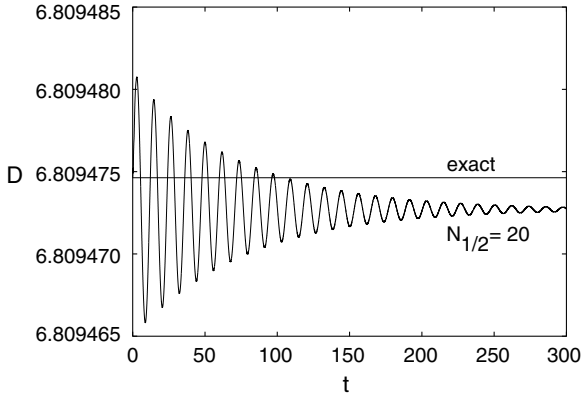

Fig. 3. Numerically generated detonation velocity, D versus t, using the high order shock-fitting scheme, $E = 25$, $q = 50$, $\gamma = 1.2$, with $N_{1/2} = 20$.

Table 4
Numerical accuracy of high order shock-fitting scheme

$N_{1/2}$	ΔD	r_c
20	2.13×10^{-6}	–
40	6.00×10^{-8}	5.01

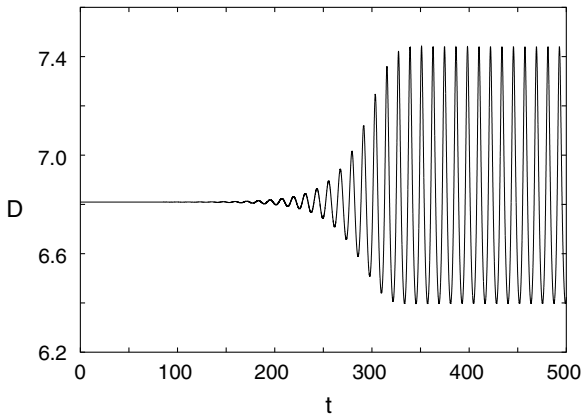

Fig. 4. Numerically generated detonation velocity, D versus t, using the high order shock-fitting scheme, $E = 26$, $q = 50$, $\gamma = 1.2$, with $N_{1/2} = 20$. Period-1 oscillations shown.

exponential growth of $D(t)$ at early times ($t < 300$). Postulating that the numerical predictions could be fit by an equation of the form

$$D(t) \sim a_0 + a_1 e^{a_2 t} \sin(a_3 t + a_4), \tag{37}$$

a least squares curve fit of the data over the range $0 < t < 100$ revealed that

$$a_0 = 6.80947239809145 \pm 7.506 \times 10^{-10}, \tag{38a}$$

$$a_1 = 0.00000643598884 \pm 4.549 \times 10^{-10}, \tag{38b}$$

$$a_2 = 0.03709980167992 \pm 7.983 \times 10^{-7}, \tag{38c}$$

$$a_3 = 0.52214295442142 \pm 8.615 \times 10^{-7}, \tag{38d}$$

$$a_4 = 0.18145671900944 \pm 7.455 \times 10^{-5}. \tag{38e}$$

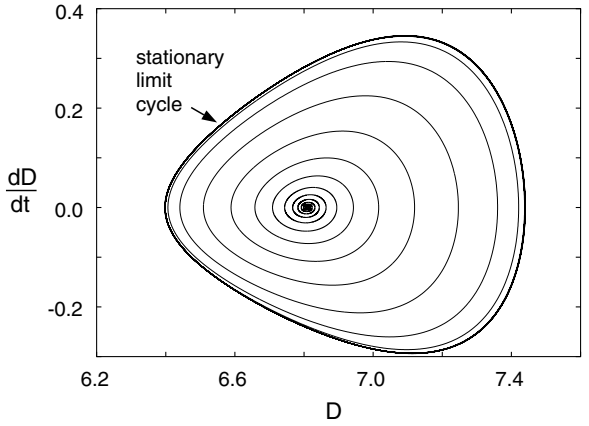

Fig. 5. Numerically generated phase portrait, dD/dt versus D, using the high order shock-fitting scheme, $E = 26$, $q = 50$, $\gamma = 1.2$, with $N_{1/2} = 20$. Period-1 oscillations shown.

Note that the growth rate a_2 and wavenumber a_3 both agree strikingly to four significant figures with the predictions of linear stability theory.

Note from Fig. 4 that the long time behavior appears to be that of a stable periodic limit cycle. One can thus infer that the non-linear effects are stabilizing the linear instability, and that the amplitude of the long time limit cycle is dictated by a balance struck between linear growth and non-linear decay. It is useful to plot the results in the phase plane, dD/dt versus D [12]. This is easily and accurately accomplished, since the shock acceleration, dD/dt, is already computed from the shock-change equation (10). Fig. 5 is the parametric plot of dD/dt versus D, where both the acceleration and velocity are known parametrically as functions of t. The solution starts at $dD/dt(t = 0) = 0$, and $D(t = 0) = D_{CJ}$. A spiral trajectory commences at this point and has a radius of curvature which increases with arc length which is indicative of the linear instability. At late times, $t > 350$, the solution has effectively relaxed to a steady cyclic behavior. It is also noted that through several numerical simulations, the linear stability boundary was determined to be located at $E = 25.265 \pm 0.005$, in excellent agreement with the prediction of linear stability theory.

4.3. Period-doubling and Feigenbaum's universal constant

As noted in [16], and later in [19], if the activation energy is increased to $E \approx 27.2$, one predicts a period-doubling phenomena, reminiscent of that predicted by the simple logistic map [33,34]. Fig. 6 shows the time history of the detonation velocity for the case $E = 27.35$. It is evident that in the long time limit, the solution

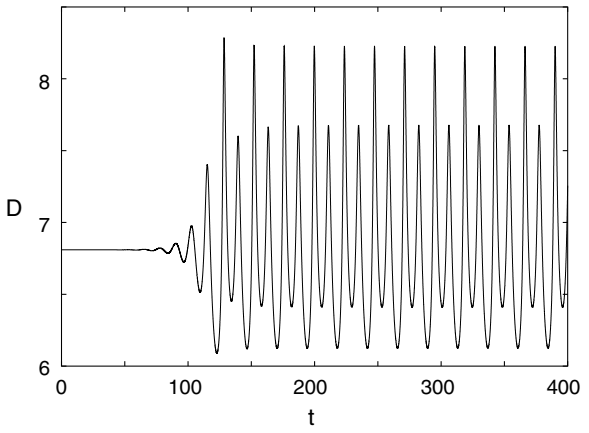

Fig. 6. Numerically generated detonation velocity, D versus t, using the high order shock-fitting scheme, $E = 27.35$, $q = 50$, $\gamma = 1.2$, with $N_{1/2} = 20$. Period-2 oscillations shown.

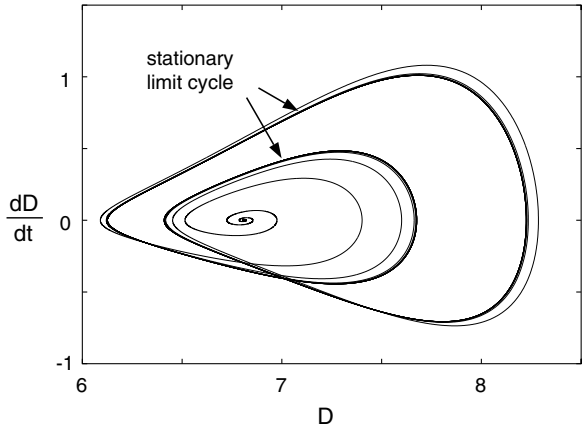

Fig. 7. Numerically generated phase portrait dD/dt versus D using the high order shock-fitting scheme, $E = 27.35$, $q = 50$, $\gamma = 1.2$, with $N_{1/2} = 20$. Period-2 oscillations shown.

Table 5
Numerically determined bifurcation points and approximations to Feigenbaum's number

n	E_n	$E_{n+1} - E_n$	δ_n
0	25.265 ± 0.005	–	–
1	27.1875 ± 0.0025	1.9225 ± 0.0075	3.86 ± 0.05
2	27.6850 ± 0.001	0.4975 ± 0.0325	4.26 ± 0.08
3	27.8017 ± 0.0002	0.1167 ± 0.0012	4.66 ± 0.09
4	27.82675 ± 0.00005	0.02505 ± 0.00025	–

possesses two distinct relative maxima, namely $D \approx 8.225$ and $D \approx 7.676$; whereas for $E = 26$, only a single relative maximum, $D \approx 7.439$ is predicted. The corresponding phase plane is shown in Fig. 7. Performing several simulations, with $N_{1/2} = 20$, to long times (up to $t = 30000$), one can bisect the region $26 < E < 27.35$, in an attempt to find the bifurcation point, i.e., the point where the single periodic cycle gives way to the period-2 solution. The activation energy at this point will be denoted by E_1. Likewise, as noted in [19], there are other period-doubling bifurcation values of E_n, where the solution transits from a period-2^{n-1} to a period-2^n. The point at which one predicts the transition from a steady solution (linear stability) to a periodic solution (period-1 solution) will be designated by E_0. These bifurcation points and the associated numerical uncertainties are given in Table 5. Also calculated are the differences between these points, $E_{n+1} - E_n$, and the relative change in the differences, δ_n:

$$\delta_n = \frac{E_n - E_{n-1}}{E_{n+1} - E_n}. \tag{39}$$

It was predicted by Feigenbaum [28,29], using models of several different physical and mathematical phenomena, that in the limit as $n \to \infty$, that δ_n approaches a universal constant, $\delta_\infty \approx 4.669201$, now commonly known as Feigenbaum's number. Table 5 shows three progressively better approximations, δ_1, δ_2, and δ_3, to δ_∞. It is seen that δ_3 is in agreement with δ_∞, with an uncertainty of 2%.

4.4. Bifurcation diagram, semi-periodic solutions, odd periods, windows and chaos

Given that the solutions obtained, even for $N_{1/2} = 20$, are so accurate and efficient to calculate, a detailed bifurcation diagram can be constructed with much greater detail than any to date. It is noted that [19] did show the first bifurcation diagram for this model, albeit with only 25 different activation energies. Here, the bifurcation diagram is constructed by sampling over a thousand different activation energies, with $25 < E < 28.8$ with $\Delta E = 0.0025$. At each value of E, the exact ZND solution is used as the initial condition. For each E, the solution is integrated to $t = 7000$, and all the relative maxima in D are recorded for

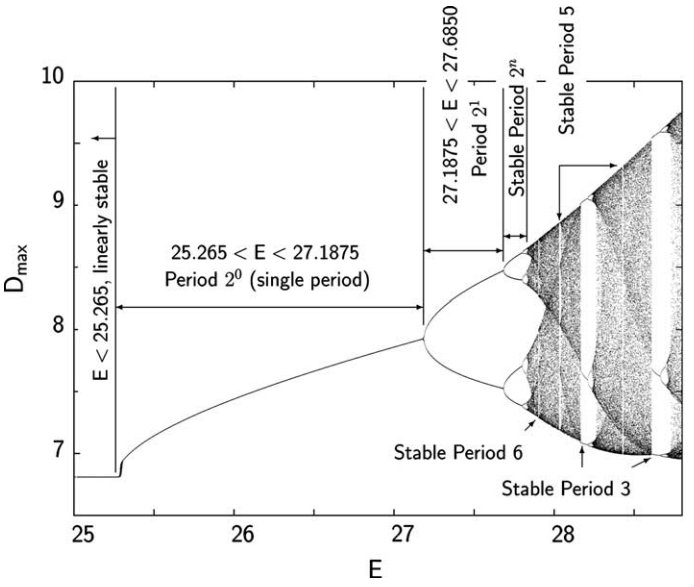

Fig. 8. Numerically generated bifurcation diagram, $25 < E < 28.8$, $q = 50$, $\gamma = 1.2$.

$5000 < t < 7000$ (i.e., the late time behavior). This composite plot of predicted, late time, relative maxima in D versus E is presented in Fig. 8. The qualitative similarities to the logistic map are striking. One clearly notices the various period-doubling bifurcations up to roughly $E_\infty \approx 27.8324$. One then notes various regions of semi-periodic behavior, and various odd-periodic regions. For example in the vicinity of $E = 28.2$, a large period-3 window opens in the bifurcation diagram; as E is increased further, the period-3 solution bifurcates. In regions where the bifurcation points are very dense, it is likely that the system has underwent a transition to chaos.

Fig. 9 gives several plots of D versus t as activation energy is increased. Specific values of E are listed in the caption. In Fig. 9(a), a period-4 solution is shown. As E is increased, the system continues a bifurcation process, and a chaotic state is realized in general. However, in (b), (c), and (d) examples are found which are within windows of order in an otherwise chaotic region. Periods of 6, 5, and 3 are found, respectively. In (e), a chaotic solution is shown. In (f) another structured solution is found with period-3.

Note that as the system becomes more chaotic, the solution remains resolved. This is because the periods are increasing, not decreasing. However, for much higher activation energies, roughly $E > 30$, higher frequency instabilities are excited, and finer resolution would be necessary. Moreover, at such high activation energies, secondary captured shocks may overtake the fitted lead shock, which would negate the advantage of the present shock-fitting method.

4.5. Asymptotically stable limit cycles

Further studies of the limit cycle behavior for detonations with

$$E \in \{26, 26.5, 27, 27.5, 28.2, 28.65\} \tag{40}$$

were also performed. In particular, two limit cycle properties were examined: the period and the average detonation speed.

The period of the limit cycle is the smallest amount of time T such that

$$\mathbf{u}(t + T) = \mathbf{u}(t). \tag{41}$$

Thus a small window in the phase plane $(D, \mathrm{d}D/\mathrm{d}t)$ is selected such that the solution trajectory passes through it once per cycle as a single valued function. Within this window, a fixed value $D = D^*$ is selected. By finding the unique times at which the solution passes through D^* for consecutive cycles, the period can be approximated. Since numerical solutions give $t(D)$ discretely, the value of t at which $D = D^*$ is found by interpolation. For the nth cycle, five data points (D, t) in the neighborhood of D^* are captured, and a Lagrange interpolating

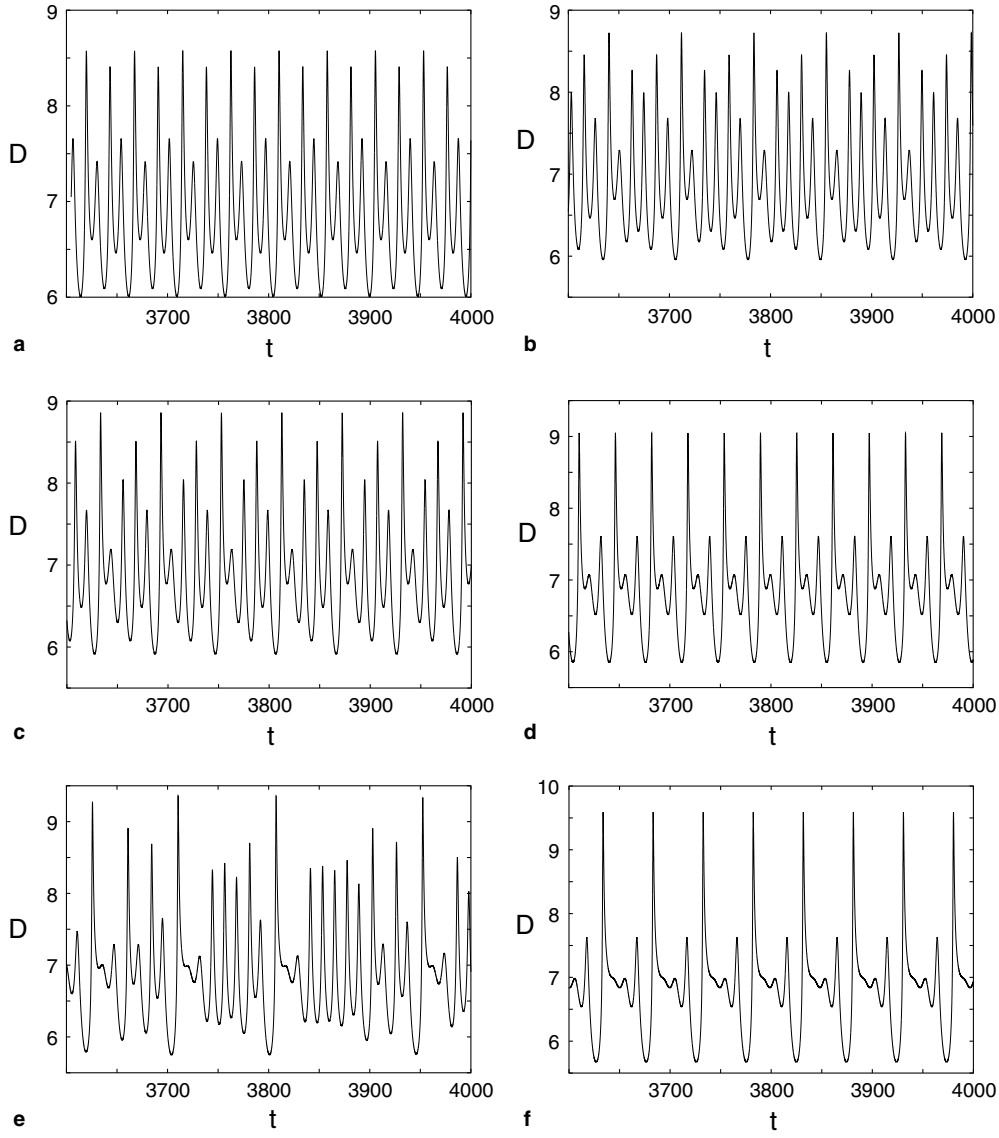

Fig. 9. Numerically generated detonation velocity, D versus t, using the high order shock-fitting scheme, $q = 50$, $\gamma = 1.2$, with $N_{1/2} = 20$: (a) $E = 27.75$, period-4, (b) $E = 27.902$, period-6, (c) $E = 28.035$, period-5, (d) $E = 28.2$, period-3, (e) $E = 28.5$, chaotic, (f) $E = 28.66$, period-3.

polynomial is passed through them. Evaluation of this polynomial at $D = D^*$ gives t_n, a fifth order approximation of the time at which the solution passed through D^* during the nth cycle. Here D^* was chosen to be D_{CJ}, and thus the period is simply

$$T = t_{n+1}(D_{CJ}) - t_n(D_{CJ}). \tag{42}$$

Having found the period, the average velocity was then computed from

$$D_{avg} = \frac{\xi_0(t_{n+1}(D_{CJ})) - \xi_0(t_n(D_{CJ}))}{T}, \tag{43}$$

where $\xi_0(t) = \xi(x = 0, t)$ is the shock location in the lab frame found from Eq. (3).

The converged period and average velocity for each activation energy in Eq. (40) are given in Table 6 for $N_{1/2} = 80$. A new and particularly interesting result is that the average detonation speed increases as E increases and only equals D_{CJ} for the linearly stable case of $E < 25.26$. This is illustrated in Fig. 10.

Table 6
Converged period and average detonation speed for $\Delta x = 0.0125$

E	Period	D_{avg}
26	11.82102781	6.810527134
26.5	11.838380175	6.811158675
27	11.877201192	6.811723287
27.5	23.790471808	6.812119710
28.2	35.859529390	6.812377052
28.65	49.514811239	6.812710499

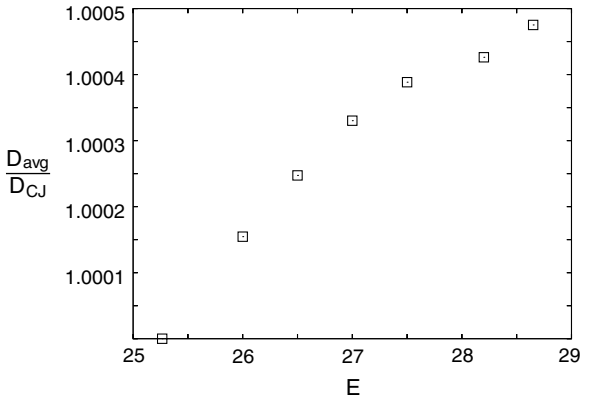

Fig. 10. Normalized average detonation velocity as a function of activation energy for selected periodic cases. For all cases, $N_{1/2} = 80$.

Table 7
Convergence rates of the limit cycle period for $E = 28.2$

Δx	Period	r_c
1/20	35.86111963	–
1/40	35.859442127	4.2648
1/80	35.859529390	4.6210
1/160	35.859532936	4.9407
1/320	35.859533052	–

Furthermore, for a single asymptotically stable value of E, both the period and its self-convergence rate can be calculated over a number of resolutions. The case of $E = 28.2$ is shown in Table 7. The period convergence rate indicates that the method is also fifth order convergent in the linearly unstable case, as anticipated from the convergence result of Table 4.

5. Conclusions

Investigation of the model one-dimensional unsteady detonation problem using shock-fitting coupled with a high order discretization scheme has clarified the behavior of linearly unstable detonations for a select range of activation energies. The resulting fifth order scheme allows for quantification of the chaotic and limit cycle behavior of the system. Bifurcation behavior and transition to chaos while varying the activation energy is demonstrated and found to be reminiscent of that governing the logistic map. In particular, the period and average detonation velocity for asymptotically stable solutions are studied, and the average detonation velocity for each case is seen to be slightly larger than the CJ speed.

The results for this simple model problem suggest that, when properly employed, shock-fitting coupled with a high order spatio-temporal discretization can yield gains in accuracy of many orders of magnitude relative to existing algorithms for certain specialized problems. Besides admitting solutions in more rapid fashion, such schemes enable existing computational resources to be used to predict new phenomena. While advances in

hardware have certainly increased computational predictive capabilities, it must be admitted that, even accounting for the unlikely continuation of Moore's Law, realization of the algorithm-driven accuracy gains achieved here by reliance on hardware improvements alone would require several years, if not decades, to achieve.

Acknowledgments

This study was performed under the auspices of the US Department of Energy. The authors thank A.R. Kasimov and D.S. Stewart for sharing their numerical solutions for various cases presented in this paper. They also thank G.J. Sharpe and M. Short for providing detailed growth rates and frequencies used in comparisons, H.D. Ng for useful discussions regarding the path to instability, and J.B. Bdzil for discussions regarding the shock-change equation.

References

[1] A.K. Henrick, T.D. Aslam, J.M. Powers, Highly accurate numerical simulations of pulsating one-dimensional detonations, in: 43rd AIAA Aerospace Sciences Meeting and Exhibit, AIAA Paper 2005-1311, 2005.
[2] S. Yungster, K. Radhakrishnan, Pulsating one-dimensional detonations in hydrogen-air mixtures, Combustion Theory and Modelling 8 (4) (2004) 745–770.
[3] J.M. Powers, S. Paolucci, Accurate spatial resolution estimates for reactive supersonic flow with detailed chemistry, AIAA Journal 43 (5) (2005) 1088–1099.
[4] C.-W. Shu, S. Osher, Efficient implementation of essentially nonoscillatory schemes for hyperbolic conservation laws, Journal of Computational Physics 77 (2) (1988) 439–471.
[5] A.K. Henrick, T.D. Aslam, J.M. Powers, Mapped weighted essentially non-oscillatory schemes: achieving optimal order near critical points, Journal of Computational Physics 207 (2) (2005) 542–567.
[6] C.B. Macdonald, Constructing high-order Runge–Kutta methods with embedded strong-stability-preserving pairs, Master's thesis, Simon Fraser University, 2003.
[7] J.J. Erpenbeck, Stability of steady-state equilibrium detonations, Physics of Fluids 5 (5) (1962) 604–614.
[8] W. Fickett, W.W. Wood, Flow calculations for pulsating one-dimensional detonations, Physics of Fluids 9 (1966) 903–916.
[9] H.I. Lee, D.S. Stewart, Calculation of linear detonation instability: one-dimensional instability of plane detonation, Journal of Fluid Mechanics 216 (1990) 103–132.
[10] A. Bourlioux, A.J. Majda, V. Roytburd, Theoretical and numerical structure for unstable one-dimensional detonations, SIAM Journal on Applied Mathematics 51 (2) (1991) 303–343.
[11] L. He, J.H.S. Lee, The dynamical limit of one-dimensional detonations, Physics of Fluids 7 (5) (1995) 1151–1158.
[12] J. Yao, D.S. Stewart, On the dynamics of multi-dimensional detonation, Journal of Fluid Mechanics 309 (1996) 225–275.
[13] M. Short, Multidimensional linear stability of a detonation wave at high activation energy, SIAM Journal on Applied Mathematics 57 (2) (1997) 307–326.
[14] G.J. Sharpe, Linear stability of idealized detonations, Proceedings of the Royal Society of London Series A – Mathematical Physical and Engineering Sciences 453 (1967) (1997) 2603–2625.
[15] P. Hwang, R.P. Fedkiw, B. Merriman, T.D. Aslam, A.R. Karagozian, S.J. Osher, Numerical resolution of pulsating detonation waves, Combustion Theory and Modelling 4 (3) (2000) 217–240.
[16] G.J. Sharpe, S.A.E.G. Falle, Numerical simulations of pulsating detonations: I. Nonlinear stability of steady detonations, Combustion Theory and Modelling 4 (4) (2000) 557–574.
[17] T.D. Aslam, A level set algorithm for tracking discontinuities in hyperbolic conservation laws II: systems of equations, Journal of Scientific Computing 19 (1–3) (2003) 37–62.
[18] A.R. Kasimov, D.S. Stewart, On the dynamics of self-sustained onedimensional detonations: a numerical study in the shock-attached frame, Physics of Fluids 16 (10) (2004) 3566–3578.
[19] H.D. Ng, A.J. Higgins, C.B. Kiyanda, M.I. Radulescu, J.H.S. Lee, K.R. Bates, N. Nikiforakis, Nonlinear dynamics and chaos analysis of one-dimensional pulsating detonations, Combustion Theory and Modelling 9 (1) (2005) 159–170.
[20] A. Majda, S. Osher, Propagation of error into regions of smoothness for accurate difference approximations to hyperbolic equations, Communications on Pure and Applied Mathematics 30 (6) (1977) 671–705.
[21] J. Casper, M.H. Carpenter, Computational consideration for the simulation of shock-induced sound, SIAM Journal on Scientific Computing 19 (3) (1998) 818–828.
[22] M.H. Carpenter, J.H. Casper, Accuracy of shock capturing in two spatial dimensions, AIAA Journal 37 (9) (1999) 1072–1079.
[23] J.M. Powers, T.D. Aslam, Exact solutions for two-dimensional reactive flow for verification of numerical algorithms, in: 43rd AIAA Aerospace Sciences Meeting and Exhibit, AIAA Paper 2005-1173, 2005, to appear in the AIAA Journal.
[24] D.A. Kopriva, T.A. Zang, M.Y. Hussaini, Spectral methods for the Euler equations: the blunt body problem revisited, AIAA Journal 29 (9) (1991) 1458–1462.
[25] G.P. Brooks, J.M. Powers, Standardized pseudospectral formulation of the inviscid supersonic blunt body problem, Journal of Computational Physics 197 (1) (2004) 58–85.

[26] D.G. Lasseigne, T.L. Jackson, M.Y. Hussaini, Nonlinear interaction of detonation/vorticity wave, Physics of Fluids A 3 (8) (1991) 1972–1979.
[27] W. Fickett, W. Davis, Detonation, University of California Press, Berkeley, CA, 1979.
[28] M.J. Feigenbaum, Quantitative universality for a class of non-linear transformations, Journal of Statistical Physics 19 (1) (1978) 25–52.
[29] M.J. Feigenbaum, The universal metric properties of nonlinear transformations, Journal of Statistical Physics 21 (6) (1979) 669–706.
[30] G.B. Whitham, Linear and Nonlinear Waves, Wiley, New York, 1974.
[31] G.-S. Jiang, C.-W. Shu, Efficient implementation of weighted ENO schemes, Journal of Computational Physics 126 (1) (1996) 202–228.
[32] R.L. Burden, J.D. Faires, Numerical Analysis, Prindle, Weber and Schmidt, Boston, MA, 1985.
[33] E.A. Jackson, Perspectives on Nonlinear Dynamics, Cambridge University Press, New York, 1991.
[34] P.G. Drazin, Nonlinear Systems, Cambridge University Press, New York, 1992.